



Numerical analysis of wavefront aberration correction using multielectrode electrowetting-based devices

MO ZOHRABI,^{1,*} ROBERT H. CORMACK,¹ CONNOR McCULLOUGH,² OMKAR D. SUPEKAR,³ EMILY A. GIBSON,² VICTOR M. BRIGHT,³ AND JULIET T. GOPINATH^{1,4}

¹Department of Electrical, Computer, and Energy Engineering, University of Colorado, Boulder, CO 80309, USA

²Department of Bioengineering, University of Colorado Anschutz Medical Campus, Aurora, CO 80045, USA

³Department of Mechanical Engineering, University of Colorado Boulder, CO 80309, USA

⁴Department of Physics, University of Colorado, Boulder, CO 80309, USA

*Mo.Zohrabi@colorado.edu

Abstract: We present numerical simulations of multielectrode electrowetting devices used in a novel optical design to correct wavefront aberration. Our optical system consists of two multielectrode devices, preceded by a single fixed lens. The multielectrode elements function as adaptive optical devices that can be used to correct aberrations inherent in many imaging setups, biological samples, and the atmosphere. We are able to accurately simulate the liquid-liquid interface shape using computational fluid dynamics. Ray tracing analysis of these surfaces shows clear evidence of aberration correction. To demonstrate the strength of our design, we studied three different input aberrations mixtures that include astigmatism, coma, trefoil, and additional higher order aberration terms, with amplitudes as large as one wave at 633 nm.

© 2017 Optical Society of America under the terms of the [OSA Open Access Publishing Agreement](#)

OCIS codes: (230.0230) Optical devices; (220.1080) Active or adaptive optics; (000.4430) Numerical approximation and analysis; (230.2090) Electro-optical devices.

References and links

1. W. R. Zipfel, R. M. Williams, and W. W. Webb, "Nonlinear magic: Multiphoton microscopy in the biosciences," *Nat. Biotechnol.* **21**(11), 1369–1377 (2003).
2. W. Denk, J. H. Strickler, and W. W. Webb, "Two-Photon laser scanning fluorescence microscopy," *Science* **248**, 73–76 (1990).
3. M. Schwertner, M. J. Booth, and T. Wilson, "Characterizing specimen induced aberrations for high NA adaptive optical microscopy," *Opt. Express* **12**, 6540–6552 (2004).
4. C. Dong, K. Koenig, and P. So, "Characterizing point spread functions of two-photon fluorescence microscopy in turbid medium," *J. Biomed. Opt.* **8**, 450–459 (2003).
5. A. L. A. Mascaro, L. Sacconi, and F. S. Pavone, "Multi-Photon nanosurgery in live brain," *Frontiers in Neuroenergetics* **2**, 21 (2010).
6. P. Godara, A. M. Dubis, A. Roorda, J. L. Duncan, J. Carroll, "Adaptive optics retinal imaging: Emerging clinical applications," *Optom. Vis. Sci.* **87**, 930–941 (2010).
7. B. L. Ellerbroek, "First-order performance evaluation of adaptive-optics systems for atmospheric-turbulence compensation in extended-field-of-view astronomical telescopes," *J. Opt. Soc. Am. A* **11**, 783–805 (1994).
8. K. Wang, W. Sun, C. T. Richie, B. K. Harvey, E. Betzig, and N. Ji, "Direct wavefront sensing for high-resolution in vivo imaging in scattering tissue," *Nat. Commun.* **6**, 7276 (2015).
9. C. Wang and N. Ji, "Characterization and improvement of three-dimensional imaging performance of GRIN-lens-based two-photon fluorescence endomicroscopes with adaptive optics," *Opt. Express* **21**, 27142–27154 (2013).
10. E. J. Botcherby, C. W. Smith, M. M. Kohl, D. Débarre, M. J. Booth, R. Juškaitis, O. Paulsen, and T. Wilson, "Aberration-free three-dimensional multiphoton imaging of neuronal activity at kHz rates," *Proc. Natl. Acad. Sci. U.S.A.* **109** 2919–2924 (2012).
11. J. W. Hardy, *Adaptive optics for astronomical telescopes* (Oxford University Press, New York, 1988).
12. J. Liang, B. Grimm, S. Goelz, and J. F. Bille, "Objective measurement of wave aberrations of the human eye with the use of a Hartmann-Shack wave-front sensor," *J. Opt. Soc. Am. A* **11**, 1949–1957 (1994).

13. J. M. Girkin, S. Poland, and A. J. Wright, "Adaptive optics for deeper imaging of biological samples," *Curr. Opin. Biotechnol.* **20**, 106–110 (2009).
 14. P. N. Marsh, D. Burns, and J. M. Girkin, "Practical implementation of adaptive optics in multiphoton microscopy," *Opt. Express* **11**, 1123–1130 (2003).
 15. P. M. Prieto, E. J. Fernández, S. Manzanera, and P. Artal, "Adaptive optics with a programmable phase modulator: applications in the human eye," *Opt. Express* **12**, 4059–4071 (2004).
 16. M. C. Roggeman, V. M. Bright, B. M. Welsh, Sh. R. Hick, P. C. Roberts, W. D. Cowan, and J. H. Comtois, "Use of micro-electro-mechanical deformable mirrors to control aberrations in optical systems: theoretical and experimental results," *Opt. Eng.* **36**, 1326–1338 (1997).
 17. M. T. Grunecisen, L. F. DeSandre, R. C. Dymale, J. R. Rotgé, and D. L. Lubin, "Compensated telescope system with programmable diffractive optic," *Opt. Eng.* **44**(2), 023201 (2005).
 18. W. C. Nelson and C. J. Kim, "Droplet actuation by electrowetting-on-dielectric (EWOD): A review," *J. Adhes. Sci. Technol.* **26**, 1747–1771 (2012).
 19. K. Mishra, D. van den Ende, and F. Mugele, "Recent developments in optofluidic lens technology," *Micromachines* **7**, 102 (2016).
 20. G. Lippmann, "Relations entre les phénomènes électriques et capillaires," *Ann. Chim. Phys.* **5**, 494 (1875).
 21. B. H. W. Hendriks, S. Kuiper, M. A. J. VAN As, C. A. Renders, and T. W. Tukker, "Electrowetting-based variable-focus lens for miniature systems," *Opt. Rev.* **12**, 255–259 (2005).
 22. S. Kuiper, and B. H. W. Hendriks, "Variable-focus liquid lens for miniature cameras," *Appl. Phys. Lett.* **85**, 1128–1130 (2004).
 23. B. N. Ozbay, J. T. Losacco, R. Cormack, R. Weir, V. M. Bright, J. T. Gopinath, D. Restrepo, and E. A. Gibson, "Miniaturized fiber-coupled confocal fluorescence microscope with an electrowetting variable focus lens using no moving parts," *Opt. Lett.* **40**, 2553–2556 (2015).
 24. C. U. Murade, J. M. Oh, D. van den Ende, and F. Mugele, "Electrowetting driven optical switch and tunable aperture," *Opt. Express* **19**, 15525–15531 (2011).
 25. R. D. Montoya, K. Underwood, S. Terrab, A. M. Watson, V. M. Bright, and J. T. Gopinath, "Large extinction ratio optical electrowetting shutter," *Opt. Express* **24**, 9660–9666 (2016).
 26. N. R. Smith, D. C. Abeyasinghe, J. W. Haus, and J. Heikenfeld, "Agile wide-angle beam steering with electrowetting microprisms," *Opt. Express* **14**, 6557–6563 (2006).
 27. S. Terrab, A. M. Watson, C. Roath, J. T. Gopinath, and V. M. Bright, "Adaptive electrowetting lens-prism element," *Opt. Express* **23**, 25838–25845 (2015).
 28. D. Kopp, L. Lehmann, and H. Zappe, "Optofluidic laser scanner based on a rotating liquid prism," *Appl. Opt.* **55**, 2136–2142 (2016).
 29. D. Kopp and H. Zappe, "Tubular astigmatism-tunable fluidic lens," *Opt. Lett.* **41**, 2735–2738 (2016).
 30. N. C. Lima, A. Cavalli, K. Mishra, and F. Mugele, "Numerical simulation of astigmatic liquid lenses tuned by a stripe electrode," *Opt. Express* **24**, 4210–4220 (2016).
 31. N. C. Lima, K. Mishra, and F. Mugele, "Aberration control in adaptive optics: a numerical study of arbitrarily deformable liquid lenses," *Opt. Express* **25**, 6700–6711 (2017).
 32. R. Finn, *Equilibrium capillary surfaces*, (Springer-Verlag, 1986).
 33. S.-L. Lee and Ch.-F. Yang, "Numerical simulation for meniscus shape and optical performance of a MEMS-based liquid micro-lens," *Opt. Express* **16**, 19995–20007 (2008).
 34. T. Sarpkaya, "Vorticity, free surface and surfactants," *Annu. Rev. Fluid Mech.* **28**, 83–128 (1996).
 35. S.-L. Lee and H.-D. Lee, "Evolution of liquid meniscus shape in a capillary Tube," *ASME J. Fluids Eng.* **129**, 957–965 (2007).
 36. O. D. Supekar, M. Zohrabi, J. T. Gopinath, and V. M. Bright, "Enhanced response time of electrowetting lenses with shaped input voltage functions," *Langmuir* **33**, 4863–4869 (2017).
 37. O. D. Supekar, B. N. Ozbay, M. Zohrabi, Ph. D. Nystrom, G. L. Futia, D. Restrepo, E. A. Gibson, J. T. Gopinath, and V. M. Bright, "Two-photon laser scanning microscopy with electrowetting-based prism scanning," *Biomed. Opt. Express* **8**, 5412–5426 (2017).
 38. O. Albert, L. Sherman, G. Mourou, T. B. Norris, and G. Vdovin, "Smart microscope: an adaptive optics learning system for aberration correction in multiphoton confocal microscopy," *Opt. Lett.* **25**, 52–54 (2000).
 39. M. A. A. Neil, M. J. Booth, and T. Wilson, "Closed-loop aberration correction by use of a modal Zernike wave-front sensor," *Opt. Lett.* **25**, 1083–1085 (2000).
 40. H. Hofer, L. Chen, G. Y. Yoon, B. Singer, Y. Yamauchi, and D. R. Williams, "Improvement in retinal image quality with dynamic correction of the eye's aberrations," *Opt. Express* **8**, 631–643 (2001).
 41. J. Porter, A. Guirao, I. G. Cox, and D. R. Williams, "Monochromatic aberrations of the human eye in a large population," *J. Opt. Soc. Am. A* **18**, 1793–1803 (2001).
 42. W. Zheng, Y. Wu, P. Winter, R. Fischer, D. D. Nogare, A. Hong, C. McCormick, R. Christensen, W. P. Dempsey, D. B. Arnold, J. Zimmerberg, A. Chitnis, J. Sellers, C. Waterman, and H. Shroff, "Adaptive optics improves multiphoton super-resolution imaging," *Nat. Methods* **14**, 869–872 (2017).
-

1. Introduction

Wavefront aberration is one of the major challenges for many optical systems. Aberrations can be caused by optical elements in the system, as well as by samples or the atmosphere. Their presence reduces resolution and contrast, and correction is essential for diffraction-limited performance. In multiphoton microscopy, used for three-dimensional imaging of biological specimens [1, 2], the emitted signal has a power law dependence on excitation intensity and aberrations greatly affect the imaging depth. For instance, a specimen under investigation for *in vivo* two-photon imaging can cause wavefront distortion, leading to poor imaging contrast [3]. Aberrations degrade the point-spread function (PSF) and can produce a weak fluorescence signal that will constrain the maximum achievable imaging depth [4]. Other areas that stand to benefit from aberration correction include laser ablation of tissue for laser surgery [5], retinal imaging in visual optics [6] and astronomy, where atmospheric turbulence can be problematic [7].

For both microscopy and astronomy, aberration correction can be performed directly by wavefront sensing, or indirectly, by optimizing the return signal [8–10]. Adaptive optics techniques have been developed to both characterize and correct wavefront aberrations [11–14]. Current technologies include spatial light modulators (SLM) [15] and deformable mirrors (DM) [16]. Recent studies show that deformable mirrors can improve the point-spread function, signal-to-noise, and imaging depth in multiphoton microscopy of the mouse cortex [8]. In a telescope system, a spatial light modulator can be used as an adaptive optical element to correct atmospheric turbulence-induced aberrations [17].

An attractive alternative is offered by adaptive optical elements based on the electrowetting principle [18–20]. This allows the control of the shape of a liquid droplet or a liquid-liquid interface on a dielectric surface through an applied voltage. The Lippman-Young equation [18–20] can be used to quantify the relationship between applied voltage and liquid curvature. The contact angles will be determined by the balance in surface tension at each interface and can be described by the Lippman-Young equation, $\cos \theta = \cos \theta_o + (\epsilon \epsilon_o / 2 \gamma d) V^2$, where θ is the contact angle upon applying a voltage V , θ_o is the initial contact angle without any applied voltage, ϵ and d are the effective dielectric constant and thickness of the dielectric layers, and γ is the surface tension of the liquid-liquid interface. Electrowetting devices are transmissive, compact, low power, and simple to fabricate. They are often implemented in a cylindrical cavity filled with two liquids, where an applied voltage through a dielectric changes the curvature of the liquid-liquid interface. Electrowetting-on-dielectric (EWOD) is a versatile technology, and devices have been used as variable focus lenses in cameras [21, 22] and microscopy [19, 23], as optical switches [24, 25], and as beam scanners [26–28]. EWOD tunable lenses use a single electrode, while devices implemented for beam scanning (tunable liquid prisms) benefit from two or more electrodes [26–28]. Extending device design to multiple electrodes enables generation of a custom surface shape at the liquid-liquid interface [29, 30]. These devices can be used to correct both on- and off-axis aberrations in an optical system. Recent studies of multielectrode devices have focused on astigmatism correction [29, 30]. In addition, liquid lens, using an array of one hundred addressable electrodes, has been studied numerically to correct individual Zernike modes [31] in a single device. However, our simple approach reveals the capability to implement multielectrode electrowetting devices to correct a large group of on- and off-axis aberrations. We have combined two multielectrode devices and a fixed lens to enable generation of a significantly more versatile liquid-liquid interface than from a single device. We have used Strehl ratio as a criterion to quantify the imaging quality of the design. The Strehl ratio is defined as the ratio of the image irradiance at the diffraction focus with aberration relative to an unaberrated point-spread function. A Strehl ratio of one indicates diffraction-limited performance, which produces excellent image quality.

In this study, we present numerical simulations of a simple and agile aberration correction system. The design involves two EWOD devices and a fixed lens (described in Section 2). The

liquid-liquid interface of a multielectrode device is modeled by solving the Young-Laplace equation [32–35]. We validate these surfaces against a full 3D computational fluid dynamics (CFD) simulations in COMSOL Multiphysics (using the Laminar two-phase flow model). Next, the simulated surfaces are imported into Zemax to calculate the optical performance of our design, in particular, the wavefront aberration correction. To correct a given input aberration, we implemented the genetic algorithm to vary the voltages applied to the multielectrode device. The point-spread function in our optical design is used as a feedback for the optimization algorithm in a closed loop. Here, we present the ability to correct multiple input aberrations using two multielectrode devices. The results of correcting three different input aberration examples (including astigmatism, coma, trefoil, and higher order aberration terms) are discussed in detail and show large improvement in point-spread function and Strehl ratio, compared with the uncorrected cases.

2. Geometrical configuration and numerical methods

The geometric configuration used in our simulation is based on our actual EWOD lenses and prisms [25, 27, 36, 37]. The devices are constructed in cylindrical glass tubes with ITO sidewall electrodes patterned using a 3D printing-assisted shadow masking technique. Parylene HT ($\sim 1 \mu\text{m}$) is used as the dielectric and Teflon ($\sim 500 \text{ nm}$) as the hydrophobic layer. The ground electrode, consisting of an annular Ti/Au/Ti (20 nm/500 nm/20 nm) layer, is patterned on a 10-mm diameter optical window. The optical window is epoxy bonded to the cylindrical glass tube and has a clear aperture of 3.75 mm. Two immiscible liquids (1% sodium dodecyl sulfate aqueous solution and dodecane) are sequentially filled into the device followed by placing an optical window on top of the device. The design of these multielectrode devices are based on our previous work [36], where 28 V applied voltage corresponds to a contact angle of 90° with initial contact angle of 155° at 0 V. In this work, we numerically simulate the liquid-liquid interface of a multielectrode device based on the fabrication process described here for aberration correction scheme.

The configuration of such a device is modeled in COMSOL Multiphysics and shown in Fig. 1(a). The simulation, using time-dependent 3D CFD (the Laminar two-phase flow model in COMSOL Multiphysics), is performed to evaluate the liquid-liquid surface interface. Our previous study of electrowetting devices, with a similar geometry [36], showed excellent agreement between the 3D CFD COMSOL simulation and experiment. An example of an eight-electrode device is shown in Fig. 1(b). The equilibrium surface is shown, after applying 28 V to electrodes 2, 8, and 5, while keeping other electrodes at 18 V. For visualization, the oil (top liquid) is hidden. Subsequently, the liquid-liquid interface shape is extracted from the simulation to validate the ability to correct both on- and off-axis aberrations [see Fig. 1(c)]. The wavefront can be decomposed into a set orthonormal Zernike polynomials. We have used 44 Zernike polynomials to perform a least-squares fit to the liquid-liquid interface extracted from the simulation. Initially, a larger set of Zernike polynomials had been used to repeat the least-squares fit. However, the wavefront RMS errors converged after using 44 Zernike polynomials. Figure 1(d) and (e) show the contour plot of the Zernike fit and the corresponding Zernike polynomial coefficients, respectively. The wavefront RMS errors are similar between the liquid-liquid surface extracted from the simulation and the Zernike polynomial fit. The simulation also shows the ability to correct both on- and off-axis aberrations, due to the broken symmetry around the device center.

In addition to the time-dependent COMSOL simulation, we have modeled the curvature of the meniscus between the two liquids using the Young-Laplace equation [32–35]. The model is based on the energy minimization principle and does not account for any transient effects. By solving the Young-Laplace equation, we can describe the equilibrium shape of a liquid-liquid interface for a given initial and final condition. The partial differential equation (PDE) toolbox in MATLAB is used to solve the equation for the geometry shown in Fig. 1(a). The steady-state contact angles were experimentally determined [36] to be 155° with no applied

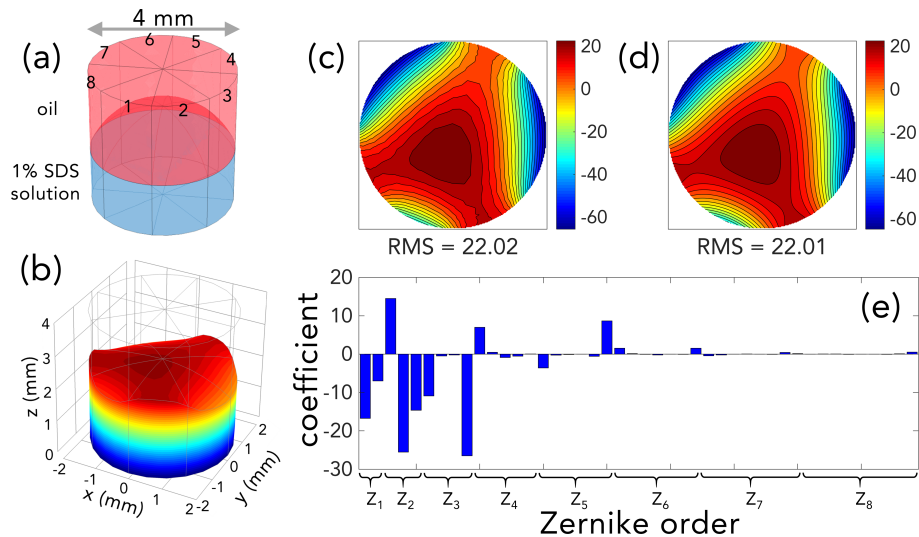


Fig. 1. (a) Simulation setup for 8-electrode device. We model a 4-mm diameter cylindrical device filled with 1% SDS solution and oil. The electrodes are labeled by numbers. (b) Simulation of the 8-electrode device after applying 28 V to electrode 2, 8, and 5, while keeping other electrodes at 18 V. (c) Contour plot of the liquid-liquid interface extracted from the simulation. (d) and (e) Zernike polynomial least-squares fit and the corresponding coefficients of wavefront aberrations.

voltage and 90° at 28 V. The contact angle, γ , variation versus the applied voltage is fitted to the Lippmann-Young's equation [19, 20] and used as a boundary condition in the Young-Laplace equation, $\nu \cdot (\nabla u / (1 + |\nabla u|^2)^{1/2}) = \cos \gamma$, where $u(x, y)$ is the liquid-liquid interface surface, ν is the unit exterior normal, and γ be the angle between the surface and the cylinder wall [32]. One practical limitation of EWOD devices is contact angle saturation [18] which restricts the contact angle tuning of these devices. The liquid-liquid surface profile is controlled by geometry of the boundaries (voltages on the electrodes); hence, using two multielectrode devices with different voltage configuration enhances the ability to produce more diverse surface profiles.

Solving the Young-Laplace equation results in an equilibrium surface between the liquid-liquid interface. The surface is in good agreement with three-dimensional CFD COMSOL simulations, which validates our results. Figure 2 shows an example of a surface extracted from the MATLAB and COMSOL simulations of an eight-electrode device with 2-mm diameter and voltage configurations of, $V = [28, 20, 28, 20, 20, 20, 28, 20]$ V on the eight electrodes. We compared the Young-Laplace method to the 3D CFD COMSOL simulation by examining the residuals. These two numerical methods show good agreement despite different discretization. The Young-Laplace and 3D CFD methods use different meshing parameters (3D CFD simulation uses adaptive meshing, while the 2D MATLAB simulation uses regular meshing), and the residues of the two simulations for various voltage configurations are within $\sim 2\%$ at the edges, indicating good agreement. Additionally, the two simulations match each other well in the center, with relative error of only 0.4% (numerical roundoff). To optimize our devices for aberration correction, we solve the Young-Laplace equation numerically using the PDE toolbox in MATLAB, as this method is computationally efficient and allows for multiple iterations. The optical design for aberration correction using multielectrode EWOD devices is shown in Fig. 3.

Our design is composed of two multielectrode EWOD devices, preceded by a single positive fixed lens (effective focal length of 16.6 mm). Since the multielectrode EWOD lenses all have negative power, to preserve a focal plane, we have to add a positive power to the system using the

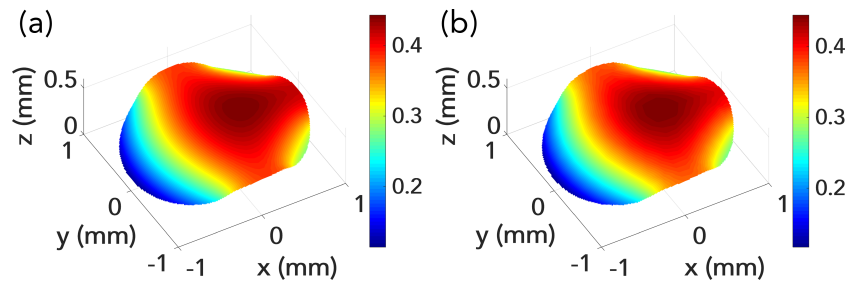


Fig. 2. (a) Liquid-liquid interface calculated by solving Young-Laplace equation in MATLAB for a 8-electrode device, 2-mm diameter, and voltage configurations, $V = [28, 20, 28, 20, 20, 20, 28, 20]$ V. The colors represent the height if the liquid-liquid interface in mm. (b) Liquid-liquid interface extracted from 3D computational fluid dynamics simulation in COMSOL for a similar device with the same voltage configuration. The two simulations agree well with each other. The residue of the two surfaces has a maximum relative error of 2% due to the two different meshes used in the simulations. The small differences are only at the edges of the circular meshes.

fixed lens. The two multielectrode devices correct the input aberration by generating deformed sphere-shaped surfaces, obeying the constraints of the Lippmann-Young induced boundary conditions. This is the main principle of our design. The resulting wavefront is imaged using a paraxial lens. The input aberration is introduced to the system before the fixed lens, as labeled in Fig. 3. Using two multielectrode devices enables us to generate a more versatile liquid-liquid interface than from a single device, allowing us to correct a larger group of input aberrations. The schematic of this design without input aberration is shown in Fig. 3.

The liquid-liquid interfaces extracted from the Young-Laplace solution are imported to the design shown in Fig. 3. In this example, device 1 and 2 are only two-electrode devices. Device 1 has sidewall voltages of 20 and 25 V. The sidewall voltages are reversed on device 2 to change the tilt angle as depicted in Fig. 3. Lastly, we use a paraxial lens to check the beam quality in the image plane. To correct a given input aberration, we model the liquid-liquid surface of each electrowetting device, using a set of random voltages. We implement a genetic algorithm (GA) to optimize the design and find the most desirable voltages for a given input aberration. The calculated surfaces are imported into Zemax and the Strehl ratio of the optical setup (one measure of optical image quality) is evaluated, and used as a feedback to the genetic algorithm in MATLAB. This single value number can be used as a feedback parameter for the optimization process and is a good measure of image quality improvement from aberration correction [38–40]. The closed-loop optimization process finds the best sets of voltages that can correct the input aberrations at the imaging plane. In addition to Strehl ratio (calculated from the point-spread function in Zemax), we have also evaluated the imaging efficiency of our design. This will ensure that the input rays are not eliminated in the optimization process (*ie.* escape system due to a large tilt in the liquid-liquid interfaces). The fitness function used for the optimization is defined as, $fitness = \sqrt{(1 - STRH)^2 + (1 - IMAE)^2}$. $STRH$ and $IMAE$ are two operands in Zemax corresponding to Strehl ratio and imaging efficiency, respectively. A Strehl ratio of one corresponds to an aberration free, ideal optical system and an imaging efficiency of one ensures that no rays are lost on the imaging plane. By minimizing the fitness function, using the GA, we find the optimum sets of voltages to correct the given input aberration.

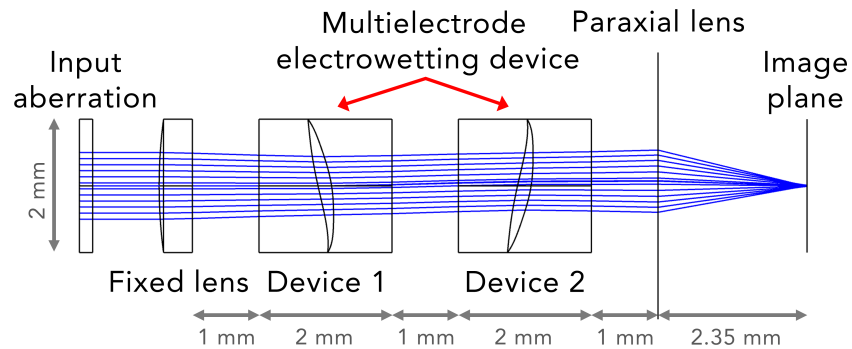


Fig. 3. Schematic optical design for wavefront aberration correction, using two multi-electrode EWOD devices, preceded by a single fixed lens (effective focal length 16.6 mm). The liquid-liquid interface is imported into Zemax through the Zemax grid sag function. Next, ray tracing is performed on the imported surfaces. The corresponding Strehl ratio and imaging efficiency are evaluated at the image plane. The fitness function, $fitness = \sqrt{(1 - STRH)^2 + (1 - IMAE)^2}$, is used as a feedback for the genetic algorithm in MATLAB. *STRH*: Strehl ratio. *IMAE*: Imaging efficiency. Imaging efficiency ensures that the input rays are not eliminated in the optimization process. Device 1 and 2 are two multi-electrode devices in our design. In this example, device 1 and 2 have 2 electrodes each to show the tilt caused by these devices. The liquid-liquid surface in this example corresponds to sidewall voltages of 20 and 25 V on device 1. The voltages are reversed for device 2, as can be seen by the opposite tilt shown in the figure.

3. Results and discussion

3.1. Astigmatism

Three different input cases containing multiple aberrations are studied. The first example uses astigmatism, one of the most common aberrations found in optical systems, corresponding to the fifth and sixth Zernike coefficients, with realistic values of astigmatism ($1 \mu\text{m}$, 1.57 wave at 633 nm for Z_5 and Z_6). Literature shows that this is reasonable assumption [41,42]. Measurements carried out on the wavefront aberration of both eyes for a large population of human subjects found that astigmatism aberrations are below $0.5 \mu\text{m}$ [41]. Multiphoton super-resolution imaging used to study aberrations through a polyacrylamide gel and a curved glass surface concluded

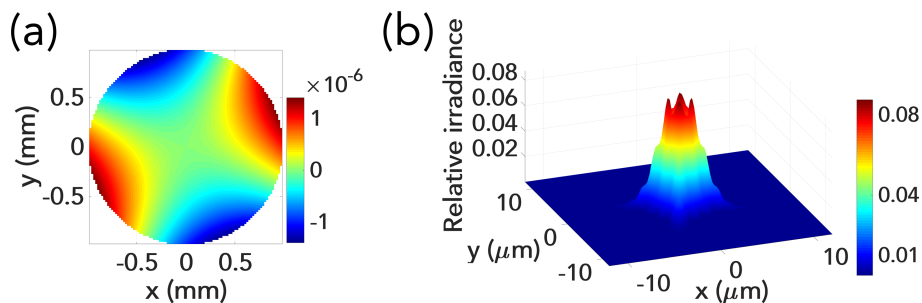


Fig. 4. PSF, point spread function. (a) Input aberrations composed of 0° and 45° astigmatism with amplitude of $1 \mu\text{m}$ (1.57 wave at $\lambda=633 \text{ nm}$). (b) The corresponding PSF after imaging the input aberration through a paraxial lens with a focal length of 2 mm. The Strehl ratio of an ideal diffraction limited beam is 1, however, the astigmatism introduced here results in a Strehl ratio of 0.086.

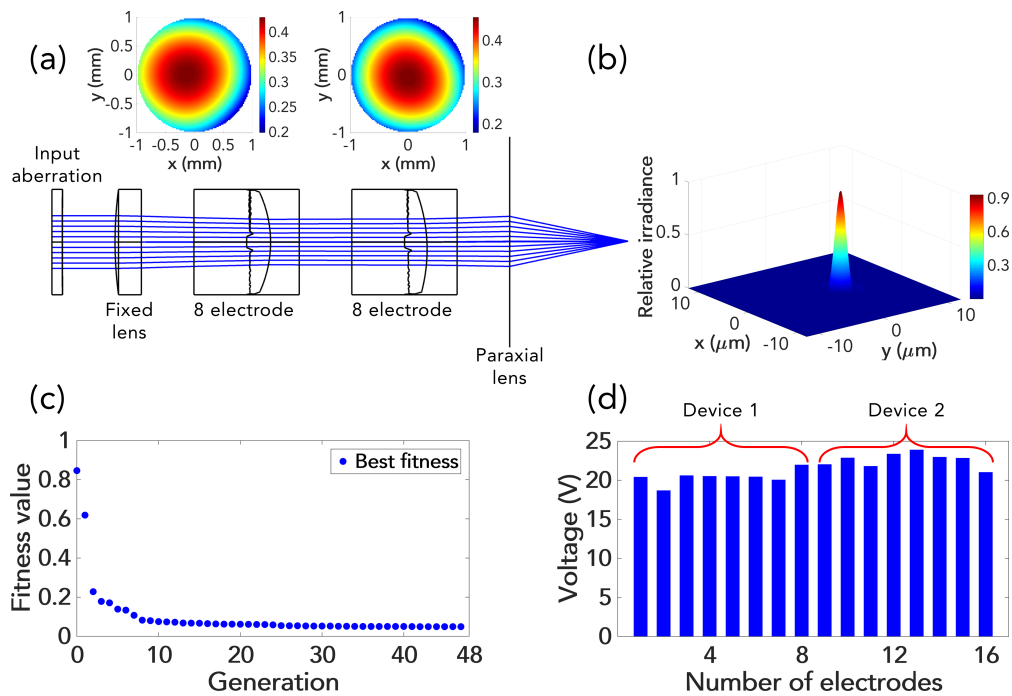


Fig. 5. GA, genetic algorithm. PSF, point spread function. (a) Astigmatism aberrations shown in Fig. 4 are used as an input for our optical design. After GA optimization, the optimum liquid-liquid surfaces are shown for both 8-electrode devices. (b) The corresponding PSF is plotted on the imaging plane with a Strehl ratio of 0.95. The result shows good correction of the input aberration and reach diffraction-limited performance. (c) Evolution of the fitness score for every generation is graphed. (d) The corresponding optimum voltages after optimization are plotted versus electrode number for both devices.

that the astigmatism coefficients were smaller than $0.3 \mu\text{m}$ [42]. More recently, astigmatism aberrations have been studied and corrected in a single optofluidic devices with amplitudes up to $3 \mu\text{m}$ [29, 30]. Figure 4 shows the result of imaging a wavefront with 0° and 45° astigmatism through a paraxial lens. The astigmatism results in a degraded Strehl ratio of 0.086 (an ideal diffraction-limited beam has a Strehl ratio of 1). The resulting distorted PSF does not allow for diffraction-limited focusing and degrades imaging contrast and resolution.

We have used astigmatism aberration as an input to the optical design showed in Fig. 3. A 1-mm diameter beam is propagated through the optical design with a central wavelength of 633 nm. Two 8-electrode devices are implemented in the simulation. In order to find the best liquid-liquid surface to correct the input aberration, 16 voltages have to be optimized (two 8-electrode devices). The GA population size of 40, with 45 generations, has been used for the optimization. The result of the optimization process is shown in Fig. 5. The optimum liquid-liquid surfaces are shown on top of 8-electrode devices, in the optical design schematic [see Fig. 5(a)]. The PSF shows great improvement, compared with the case of Fig. 4(b). A Strehl ratio of 0.95 results in a nearly diffraction-limited beam. Evolution of the fitness score for every generation is shown in Fig. 5(c). The fitness score converges to zero, corresponding to a Strehl ratio and an imaging efficiency of one. Our result shows the imaging efficiency of one with a Strehl ratio of 0.95. The corresponding optimum voltages after optimization are plotted in Fig. 5(d) for both devices. We should note that the optimization on the given input astigmatism aberration is performed using two 4-electrode devices, and the results converge to a Strehl ratio of 0.92

with an imaging efficiency of one. Using two 8-electrode devices improves the Strehl ratio to 0.95. We have repeated the optimization process using two 16-electrode devices and the Strehl ratio did not improve any further showing the result has converged to an optimum Strehl ratio. Lastly, although the astigmatism is eliminated, as shown by the Strehl ratio improvement of 0.95, a tip-tilt aberration, caused by the two multielectrode devices, is present in the imaging plane and results in a shift of the PSF. Cross-talk between Zernike modes exists because the aberration correction is not performed at the conjugate plane. However, we expect this effect to have minimal impact on image quality.

3.2. Random aberrations: 7 Zernike terms

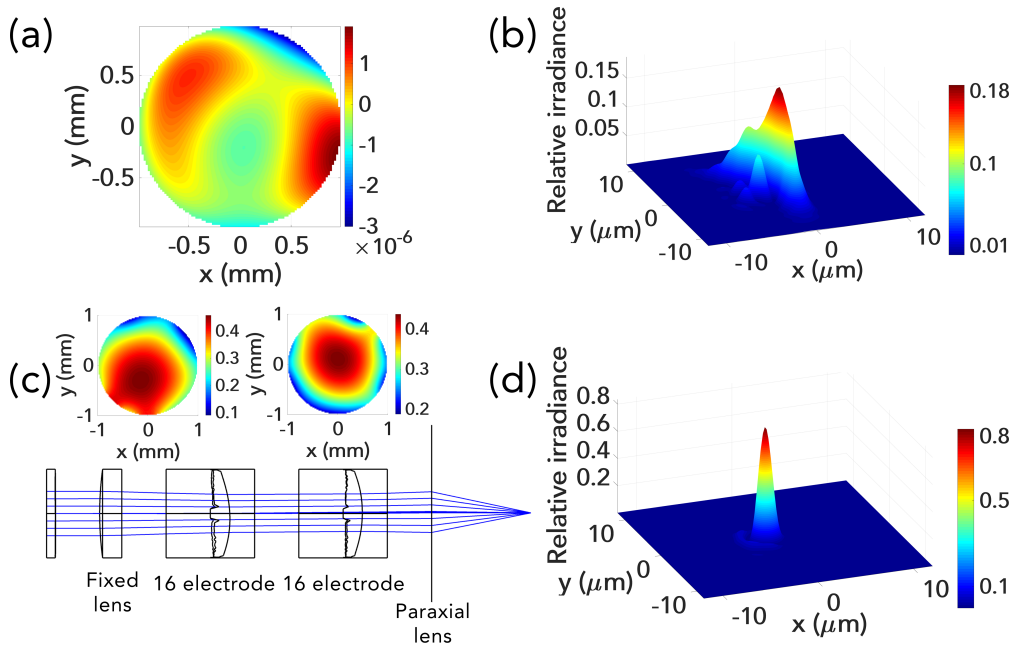


Fig. 6. PSF, point spread function. (a) Input aberration composed of two astigmatism, two coma, and two trefoil terms as well as one spherical aberration term (Z_5 to Z_{11}). (b) The corresponding the PSF is plotted after focusing through a paraxial lens with a focal length of 2 mm, with a Strehl ratio of 0.187. (c) The optimum liquid-liquid surfaces are shown for both 16-electrode devices. (d) The PSF is plotted on the imaging plane with a Strehl ratio of 0.834. The Strehl ratio shows a significant improvement of the PSF.

In the second case, we demonstrate the capability of our simple technique with seven random Zernike terms. We use the fifth through eleventh Zernike coefficients, which include: two astigmatism, two coma, and two trefoil terms as well as one spherical aberration term (does not include tip/tilt and defocus Zernike terms). The randomly generated Zernike terms were restricted in amplitude to $\pm 1 \mu\text{m}$, with values of, Z_5 : 0.97, Z_6 : -0.88, Z_7 : 0.35, Z_8 : -0.64, Z_9 : -0.632, Z_{10} : 0.74, and Z_{11} : 0.34 μm . The results of adding up these Zernike terms are shown in Fig. 6(a). Propagating a 1-mm beam through this input aberration results in a PSF with a Strehl ratio of 0.187, as shown in Fig. 6(b). Such a poor PSF is a non-starter for two-photon microscopy. We have used the optical design described in Fig. 3, in conjunction with GA optimization to correct this input aberration, using two 16-electrode devices. The resulting surfaces from GA optimization with a population size of 60, and 70 generation runs are shown in Fig. 6(c). The PSF is depicted in Fig. 6(d), with a Strehl ratio of 0.834 and an imaging efficiency of one. Initially, the

input aberration was optimized for two 8-electrode devices and the results converge to a Strehl ratio of 0.8. Using two 16-electrode devices improves the Strehl ratio to 0.834. A larger number of electrodes may improve the Strehl ratio further. However, finding the global minimum with a large number of unknown variables requires large numerical optimization times. Our aberration correction method, based on liquid multielectrode devices, shows significant improvement in the Strehl ratio. As described earlier, multiphoton microscopy has a strong dependence on the quality of the PSF of the scanning source. Thus, improving the PSF results in a stronger emitted signal and deeper scan depth. In our case the emitted two-photon signal can be improved ~ 20 times (ratio of the Strehl ratio squared).

3.3. Aberration of gradient index (GRIN) lenses used in two-photon fluorescence endomicroscope imaging: 13 Zernike terms

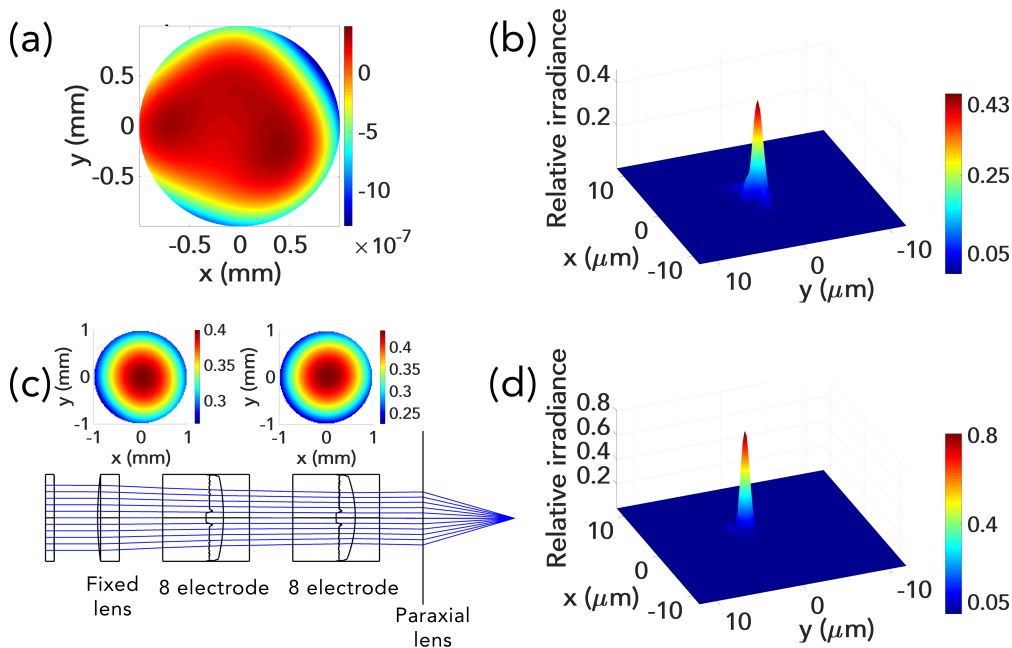


Fig. 7. PSF, point spread function. (a) Input aberration composed of tip, tilt, defocus, astigmatism, trefoil, spherical, secondary astigmatism, and quadrafoil terms (Z_2 to Z_{14}). The amplitudes are taken from the measurements of Wang *et al.* [9] measurements of a $2\ \mu\text{m}$ fluorescence bead at a working distance of $-100\ \mu\text{m}$ [red bars in Fig. 2(e)]. (b) The corresponding PSF is plotted after focusing through a paraxial lens with a focal length of 2 mm with Strehl ratio of 0.43. (c) The optimum liquid-liquid surfaces are shown for both 8-electrode devices. (d) The PSF is plotted on the imaging plane with a Strehl ratio of 0.85.

Lastly, we have examined our design, using 13 Zernike terms from the measurement carried out by Wang *et al.* [9] with a gradient index (GRIN) lenses in two-photon fluorescence endomicroscope imaging. The input aberration is extracted from the red bars in Fig. 2(e) [9], corresponding to measurements of a $2\ \mu\text{m}$ fluorescence bead at a working distance of $-100\ \mu\text{m}$. We have digitized the Zernike coefficients amplitudes and used them as an input in our simulation. Our simulation is composed of tip, tilt, defocus, astigmatism, trefoil, spherical, secondary astigmatism, and quadrafoil terms (Z_2 to Z_{14}). Adding these terms results in an aberration depicted in Fig. 7(a). Using a 1-mm diameter beam results in minimal distortion of the PSF. Propagating a 1.5-mm diameter beam through this aberration and focusing it using a paraxial lens results in a Strehl

ratio of 0.43, shown in Fig. 7(b). To correct the aberration, we run the GA optimizer, using two 8-electrode devices. The optimum solution is found, using the GA with a population size of 60, and 50 generations. The optimum liquid-liquid surfaces of two 8-electrode device interfaces are plotted in Fig. 7(c). The cylindrical symmetry of these surfaces is broken due to the asymmetric input aberrations. The corresponding PSF on the imaging plane is graphed in Fig. 7(d) with an improved Strehl ratio of 0.85. Optimization with more electrodes (*i.e.* 16) yields no improvement, with identical liquid surfaces and PSF to the 8-electrode case [see Fig. 7(d)]. Our results show that adaptive electrowetting technology with multiple electrodes can be used to compensate for aberrations of a GRIN lens and extend the depth of focus in biological tissue imaging.

4. Conclusion

Numerical simulations were performed to investigate the ability to correct wavefront aberrations using multielectrode EWOD devices. We performed a full 3D computational fluid dynamics (CFD) simulation (using the Laminar two-phase flow model in COMSOL) to predict the equilibrium shape of eight- and sixteen-electrode EWOD devices. In addition, we have solved the Young-Laplace equation in MATLAB to describe the equilibrium shape of a liquid-liquid interface for a given initial and final condition. The liquid-liquid interface from 3D CFD calculation is compared with the Young-Laplace solutions and the results show good agreement. To investigate the ability to correct wavefront aberrations, a new optical design is constructed using two multielectrode EWOD devices and the liquid-liquid surfaces were imported into Zemax, an optical design program. The PSF is evaluated through ray tracing in Zemax. We used a genetic algorithm to optimize the liquid-liquid interface by using a Strehl ratio and imaging efficiency as feedback and studied three different input aberration cases. The first case includes an astigmatism with 2 Zernike terms as an input aberration. We are able to correct the input aberrated wavefront and improve the Strehl ratio from 0.086 to 0.95. In the second example, we studied 7 random Zernike terms as an input aberration with amplitudes $\pm 1 \mu\text{m}$ and show that the aberration can be corrected, using two 16-electrode EWOD devices. Lastly, we studied 13 Zernike terms taken from the measurement reported by Wang *et al.* [9] for off-axis aberration caused by GRIN lenses in two-photon fluorescence endomicroscope imaging at $-100 \mu\text{m}$ depth. Our result shows a Strehl ratio of 0.85 after genetic algorithm optimization.

We have shown the benefits of implementing a multielectrode EWOD device as an adaptive optical element for aberration correction and beam shaping in optical systems. These devices are capable of correcting multiple low and high-order aberrations and can be realized in a variety of sizes with a large number of electrodes. The demonstration of multielectrode adaptive optical elements based on electrowetting principle for aberration correction shows the potential of this technology. Implementing this method to improve the wavefront through a random scattering medium is important in areas such as surgery, free space and fiber-coupled microscopy, imaging, and astronomy.

Funding

Office of Naval Research (ONR) N00014-15-1-2739; National Science Foundation (NSF) (IDBR) DBI-1353757; NSF (NCS-FO) CBET-1631704; National Institutes of Health (SPARC) OT2OD023852; University of Colorado Boulder Libraries Open Access Fund.

Acknowledgments

The authors would like to acknowledge Wei Yang Lim (Univ. of Colorado Boulder) for fruitful discussions. Publication of this article was funded by the University of Colorado Boulder Libraries Open Access Fund.